Effects of defects on thermoelectric properties of carbon nanotubes

Masato Ohnishi, Takuma Shiga, and Junichiro Shiomi*
The University of Tokyo, Department of Mechanical Engineering, Hongo 7-3-1, Bunkyo-ku, Tokyo 113-8656, Japan
(Received 19 November 2016; published 6 April 2017)

Carbon nanotubes (CNTs) have recently attracted attention as materials for flexible thermoelectric devices. To provide a theoretical guideline of how defects influence the thermoelectric performance of CNTs, we theoretically studied the effects of defects (vacancies and Stone-Wales defects) on their thermoelectric properties; thermal conductance, electrical conductance, and Seebeck coefficient. The results revealed that the defects most strongly suppress the electron conductance, and deteriorate the thermoelectric performance of a CNT. By plugging in the results and the intertube-junction properties into the network model, we further show that the defects with realistic concentrations can significantly degrade the thermoelectric performance of CNT-based networks. Our findings indicate the importance of the improvement of crystallinity of CNTs for improving CNT-based thermoelectrics.

DOI: 10.1103/PhysRevB.95.155405

I. INTRODUCTION

Over the last decades, nanoscale structures and materials have opened new possibilities to enhance thermoelectric properties. Low-dimensional structures such as PbTe [1], Bi_2Te_3 [2], and Si/Ge superlattices [3] have been shown to give rise to high Seebeck coefficient by quantum size effect [4,5]. In addition, progress in synthesizing/fabricating nanostructured materials such as nanocrystalline materials [6–9], nanowires [10], and nanoporous thin films [2,11] has provided ways to reduce thermal conductivity by boundary scattering of quasiballistic phonons [12]. Carbon nanotubes (CNTs) are promising thermoelectric materials with both of the above two merits; they are one-dimensional materials leading to the high Seebeck coefficient [13,14], and a sheet (network) consisting of CNTs is naturally a nanostructured material, where intertube junctions between CNTs reduce the thermal conductivity [15,16]. Moreover, with their flexibility, toughness, and stability, the CNT sheet can be attached to curved and movable objects [17–19] such as the human body, making CNT-based thermoelectric devices suitable for versatile applications.

While there is an increasing number of reports on improvement of thermoelectric performance of a sheet composed of CNTs or related carbon nanomaterials [20–23], the effect is often discussed based on a simplified picture that the thermoelectricity is mainly generated at the intertube junctions, and the body of the CNT has a minor contribution due to its high thermal conductivity (i.e., small temperature gradient). However, this may not be true with the presence of defects that are, in practice, omnipresent in bulk CNT samples, particularly in those synthesized by using the chemical vapor deposition (CVD) methods. The crystallinity of CNTs strongly depends on CVD growth conditions; even CNT samples prepared with the same process can differ due to subtle factors that are difficult to control, such as the remaining catalyst particles in a chamber [24].

While the introduction of defects to CNTs, in general, reduces both electrical and thermal conductivity (or conductance), previous works have shown that the electrical and thermal properties have different sensitivity to the type of defect; the extent of reduction varies with the defect types for electrical conductivity [25–28] but varies less for thermal conductivity [29–31]. Note that most of the works so far on the effect of crystal disorder such as defects and strain on the electronic transport properties have been done for metallic CNTs [25–28,32,33], and there are only a few works on semiconducting CNTs, which dominantly contribute to the thermoelectric performance of CNT sheets. In any case, this lack of correlation in defect sensitivity between electrical and thermal properties complicates the effect of defects on the thermoelectric performance, since the thermoelectric figure of merit is proportional to the ratio of electrical to thermal conductivity. It is, therefore, crucial to understand the effect of defects on the thermoelectric properties to further improve the performance of CNT-based thermoelectric devices.

A few previous studies on thermoelectric performance of defective or strained carbon nanomaterials such as CNTs and graphene nanoribbons have shown that vacancies [34] or uniaxial strain [13] deteriorate the thermoelectric performance. However, in these studies, the phonon transport properties were calculated in the fully ballistic regime with the atomic Green's function approach and did not consider diffusion of phonons, which makes the thermal conductance dependent on CNT length, and is known to be important for practical lengths in CNT sheets. In addition, lack in systematic analysis of the dependence on the CNT length and defect types makes it difficult to use the knowledge to estimate thermoelectric properties of CNT networks.

In this study, we systematically and comparatively study effects of defects, namely, vacancies and Stone-Wales (SW) defects on thermoelectric properties of CNTs. We employ nonequilibrium molecular dynamic (NEMD) simulation to discuss the effect of the CNT length on lattice thermal properties and the Green's function approach to calculate electronic transport properties. Using this knowledge, we further estimate the effect of defects on thermoelectric properties of CNT networks using a simplified model. Our calculation shows that the introduction of defects significantly deteriorates the thermoelectric performance of both individual CNTs and CNT networks because of the dominant suppression of the electron conductance.

*shiomi@photon.t.u-tokyo.ac.jp

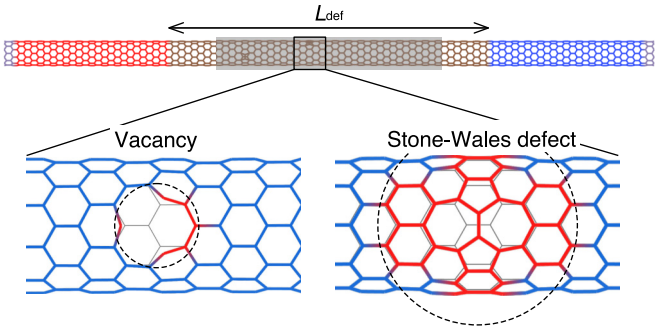

FIG. 1. Schematic of a CNT with defects: vacancy and SW defect. The defective region connects with pristine CNT leads at both ends. For the NEMD simulation, the length of the leads is half of that of the defective region ($L_{def}/2$) and are terminated by fixed layers. For the Green's function method, on the other hand, the leads are defined to be semi-infinite and periodic. Dashed circles in the bottom panels show the region in which atoms are displaced over 0.15 nm due to the introduction of defects.

II. METHODOLOGY

Semiconducting (10, 0) CNTs with a relatively small diameter, d_{cnt}(=0.78 nm), are used in this study. Small-diameter semiconducting CNTs are important for the thermoelectrics because CNTs with smaller diameters have larger thermopower, the absolute value of the Seebeck coefficient [13]. In the simulated systems, a defective region is connected with right and left leads consisting of a pristine CNT as illustrated in Fig. 1. The fine gray and bold colored lines in the bottom schematics show C-C bonds around the defects before and after the structural relaxation calculation, respectively. The red-colored bonds consist of atoms that are clearly displaced (over 0.15 Å) around a defect due to the relaxation calculation and the dashed circles indicate the region occupied by these displaced atoms. The diameters of the circle were 0.5 and 1.2 nm for the vacancy and SW defect, respectively. The length of the defective region is varied as $L_{def} = 10$, 50, and 100 nm. The defect concentration, $\sigma = N_{def}/N_{atom}$, is varied from 0% to 1.0%, where N_{def} is the number of defects (the number of removed atoms or rotated C-C bonds for the vacancy and SW defect, respectively) and N_{atom} is the number of atoms in the CNT before the introduction of defects. We introduce defects in the defective region except for both ends with the length of $0.15\,L_{def}$. While defects are placed randomly, their distance maintains a certain extent of distance from others (at least 1.0 nm) to avoid generating regions with excessive defect concentration. In the system for the NEMD calculations, the thermostated leads with the length of $L_{def}/2$ are connected with the fixed terminal layers (i.e. adiabatic boundary) consisting of a primitive unit cell. On the other hand, for Green's function calculations, the leads have a periodic and semi-infinite structure. For both calculations, relaxation calculation with the optimized Tersoff potential [35] is performed until all atomic forces become less than 0.01 eV/Å to reduce the defect-induced residual stress.

The NEMD simulations are performed using the LAMMPS package [36] with the optimized Tersoff potential, which has been developed for phonon transport in carbon nanomaterials [37]. After relaxing the CNTs in a canonical ensemble for more than 200 ps at 300 K, the temperature at the hot (cold) Nosé-Hoover (NH) thermostat is heated up to 310 K (cooled down to 290 K). After performing the NEMD simulation for 4 ns and the heat flow achieves a steady state, thermal properties such as heat current and temperature at each atom are obtained by averaging values at every time step for 2 ns. The heat current through the defective region is computed as $Q_{ave} = (Q_{hot} + Q_{cold})/2$, where Q_{hot} and Q_{cold} are the energy added to or subtracted from the hot and cold thermostats per unit time, respectively. The error between the added and subtracted energies, $|Q_{hot} - Q_{cold}|/Q_{ave}$, was up to 0.07 (less than 0.02 for most cases). The time step and damping time of thermostats are set to 0.5 and 50 fs for all simulations.

Lattice thermal conductivity κ_{lat} and conductance K_{lat} are then calculated as

$$\kappa_{lat} = \frac{Q_{ave}/A_{ring}}{|dT/dx|}, \qquad K_{lat} = \kappa_{lat} A_{ring}/L_{def}, \tag{1}$$

where x is the position along the tube axis, dT/dx the temperature gradient, and $A_{ring} = \pi d_{cnt} b$ the cross-sectional area of a CNT, with b (=0.34 nm) being the separation between graphite layers. To obtain the temperature gradient, we use the defective region except for both ends with the length of $0.1\,L_{def}$ (shaded region in Fig. 1); this means that defect is absent in the ends of the fitting region with the length of $0.05\,L_{def}$. This defect-free region allows the prevention of the generation of unusual temperature drop near the edges in the fitting region.

For the Green's function calculations, we use a tight-binding method [33], where the hopping integral for the π orbital between carbon atoms is attenuated exponentially with increasing the bond length [38]. The Green's function and the transmission function of the defected region are obtained as

$$G_{def} = [(E + i\eta) - H_{def} - \Sigma_L - \Sigma_R]^{-1}, \qquad \Theta(E) = \mathrm{tr}[\Gamma_L G_{def} \Gamma_R G_{def}^{\dagger}], \tag{2}$$

where E is the energy of the incident electron to the defective region, η is the infinitesimal, H_{def} is the Hamiltonian matrix of the defective region, $\Sigma_{L(R)}$ is the self-energy matrix of the left (right) lead, and $\Gamma_{L(R)} = i[\Sigma_{L(R)} - \Sigma_{L(R)}^{\dagger}]$. The electric current $I(V)$ and electronic thermal current $J(V)$ under the bias voltage V through the defective region are obtained using the Landauer-Büttiker formula [39]:

$$I(V) = \frac{2e}{h}\int dE\,\Theta(E)[f_L(E-\mu_L) - f_R(E-\mu_R)], \qquad J(V) = \frac{2e}{h}\int dE\,\Theta(E)[f_L(E-\mu_L) - f_R(E-\mu_R)](E-\mu), \tag{3}$$

where e is the electron charge; h is Planck's constant; $f_{L(R)}$ is the Fermi-Dirac distribution function of the left (right) lead, which is also a function of temperature; and μ is the chemical potential, which can be tuned with gating or doping. The temperature is set to 300 K in all the simulations. Under the linear response approximation, i.e., when the differences of the chemical potential, $\Delta\mu = \mu_L - \mu_R$(= eV), and the temperature difference ΔT between both leads are infinitesimally

small, we can obtain the thermoelectric properties as follows [13,16]:

the electronic conductance,

$$G_{\rm el} = -\frac{I}{\Delta V}\bigg|_{\Delta T=0} = e^2 A_0, \tag{4}$$

the Seebeck coefficient,

$$S = -\frac{\Delta V}{\Delta T}\bigg|_{I=0} = \frac{A_1}{eTA_0}, \tag{5}$$

and the electronic thermal conductance,

$$K_{\rm el} = \frac{J}{\Delta T}\bigg|_{I=0} = \frac{A_0A_2 - A_1^2}{TA_0}. \tag{6}$$

Here, A_n is defined as the following integral:

$$A_n = \frac{2}{h}\int dE\Theta(E)\left(-\frac{\partial f}{\partial E}\bigg|_{E=\mu}\right)(E-\mu)^n. \tag{7}$$

Using Eqs. (1) and (4)–(6), we can obtain the power factor, $P = S^2G_{\rm el}$, and the thermoelectric figure of merit, $Z_{\rm cnt}T = S^2G_{\rm el}/(K_{\rm lat} + K_{\rm el})$. For each defect concentration σ, electronic calculations are performed for five different random defect configurations, and the obtained electron properties [Eqs. (4)–(6)] are averaged. Note that, in case of thermal transport calculations, NEMD simulations were performed for a single configuration for each defect concentration because the sensitivity to the defect configuration is much smaller than for electrical transport properties. This was checked by analyzing five configurations for some cases of σ in 10-nm CNTs, and the resulting variations in $\kappa_{\rm lat}$ were sufficiently small (20% at most and less than 10% in most cases). This error will further diminish by fitting $\kappa_{\rm lat}$ as a function of σ.

The fundamental difference between the methods of thermal and electrical calculations is worth mentioning. In the Green's function method, the electron-phonon and electron-electron scattering are neglected because the electron mean free path (MFP) of pristine semiconducting CNTs is known to reach 200 nm at room temperature [40], which is sufficiently longer than the CNTs used in this study. The MFP is expected to be shorter due to electron-phonon or electron-electron scattering induced by the localized phonons and electrons around the defects but our calculations should be valid at least for low defect concentrations. On the other hand, in the NEMD simulation, it is important that the anharmonic phonon-phonon scatterings are considered because the contribution to thermal conductivity comes from phonons with a wide range of frequencies including those with MFPs shorter than the CNTs used in this study [41].

III. LATTICE THERMAL TRANSPORT PROPERTIES

A. Thermal conductivity of pristine CNTs

First we validate $\kappa_{\rm lat}$ obtained in this study. While $\kappa_{\rm lat}$'s of pristine (10, 0) CNTs obtained in this study are 170, 530, and 750 W/m K for $L_{\rm def}$ = 10, 50, and 100 nm, respectively, it is known that $\kappa_{\rm lat}$ of CNTs varies widely depending on different factors as follows. Salaway and Zhigilei show that the optimized Tersoff potential estimates $\kappa_{\rm lat}$ of CNTs larger than other empirical interatomic potentials [37]. In fact, $\kappa_{\rm lat}$ of a 100-nm (10, 10) CNT (950 W/m K), which is additionally calculated for this study, is larger than $\kappa_{\rm lat}$ calculated with the adaptive intermolecular reactive empirical bond order (AIREBO) potential (200 W/m K) [37], the Brenner potential (210 W/m K) [42], and the simplified Brenner potential (330 W/m K) [37,41]. While the choice of interatomic potential is still controversial, the optimized Tersoff potential is used in this study because this potential reproduces experimentally observed phonon properties of CNTs or graphite such as phonon dispersion, group velocities [43,44], and thermal conductivity more accurately [45].

Conditions of NH thermostats (length, temperature difference, and damping time) also affect the magnitude of $\kappa_{\rm lat}$ [41]. $\kappa_{\rm lat}$ of CNTs increases with the thermostat length because of the increase in the number of phonons generated in thermostats with their length, and converges when the thermostat length approaches half of $L_{\rm def}$ [41]. $\kappa_{\rm lat}$ of CNTs calculated in this study [750 W/m K for 100-nm 1 0, 0) CNT], therefore, are larger than those obtained by Cao and Qu [400 W/m K for a 100-nm (10, 0) CNT] using shorter thermostats (2–10 nm) [46]. In fact, when changing the length of the thermostat from 50 to 2 nm, we observed a 30% reduction of $\kappa_{\rm lat}$ for a 100-nm (10, 0) CNT (from 750 to 520 W/m K). In contrast, changing the damping time and the temperature difference between thermostats ($T_{\rm hot}-T_{\rm cold}$) from (50 fs, 20 K) to (1 ps, 60 K), the same conditions as those used by Sevik *et al.* [47], did not affect $\kappa_{\rm lat}$ of CNTs. Here, $\kappa_{\rm lat}$'s obtained by Sevik *et al.* are almost half of $\kappa_{\rm lat}$ obtained in this study and are comparable with $\kappa_{\rm lat}$ obtained by Salaway and Zhigilei and Cao and Qu, while the former used longer thermostats (constant at 50 nm) than those used by the latter.

To investigate the effect of thermal expansion on $\kappa_{\rm lat}$, we also compared $\kappa_{\rm lat}$ of 100-nm (10, 0) CNTs relaxed at 0 and 300 K (under *NPT* ensemble). By relaxing a CNT at 300 K, the CNT expands by 1% and its $\kappa_{\rm lat}$ is slightly (a few percentage points or less) smaller than $\kappa_{\rm lat}$ of the CNT relaxed at 0 K, which could be attributed to the phonon softening due to the thermal expansion [48]. However, this small variation of $\kappa_{\rm lat}$, which is in the range of ensemble fluctuations, cannot describe the above-mentioned variation of $\kappa_{\rm lat}$ among different studies. Therefore, the cause of the discrepancy is not clear at this point, and may be due to differences in more detailed methodology of the simulations that cannot be judged from the information available in the paper; however, further investigation of the discrepancy is beyond the scope of this paper. Nevertheless, the effect of defects on $\kappa_{\rm lat}$ of CNTs is consistent with that observed by Sevik *et al.* as will be discussed below.

B. Thermal conductivity of defective CNTs

Figure 2 shows the change in $\kappa_{\rm lat}$ of (10, 0) CNTs with different $L_{\rm def}$, 10 nm (black circle), 50 nm (blue square), and 100 nm (orange triangle), due to the introduction of (a) vacancies and (b) SW defects. Here, $\kappa_{\rm lat}(\sigma)$ can be written as $\kappa_{\rm lat}(\sigma) = c_{\rm ph}v_g\Lambda_{\rm tot}(\sigma)$ with $c_{\rm ph}$ being specific heat, v_g phonon group velocity, and $\Lambda_{\rm tot}$ phonon MFP in defective CNTs. $\Lambda_{\rm tot}$ satisfies the Matthiessen's rule: $\Lambda_{\rm tot}^{-1} = \Lambda_{\rm prist}^{-1} + \Lambda_{\rm def}^{-1}$, where $\Lambda_{\rm prist}$ and $\Lambda_{\rm def}$ are the MFPs in the pristine CNT and are induced by defects. Assuming that $c_{\rm ph}$ and v_g are independent

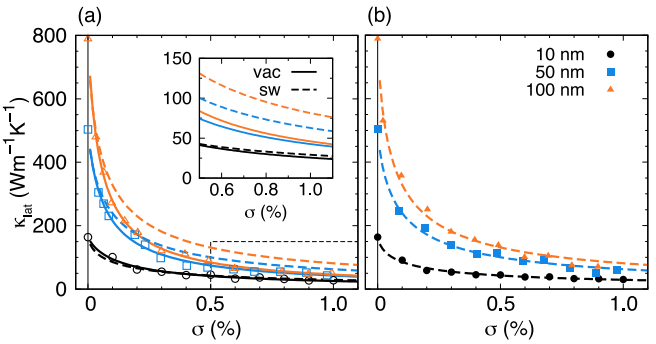

FIG. 2. Change in thermal conductivity of (10, 0) CNTs due to (a) vacancy and (b) SW defect. The symbols, black circle, blue square, and orange triangle, represent different CNT lengths, 10, 50, and 100 nm, respectively. The solid line in (a) shows the fitting line for vacancy and the broken line in (a) and (b) for SW defect. The inset in (a) shows a closeup at high defect concentration ($0.5\,\% \leqslant \sigma \leqslant 1.0\,\%$), the marked region.

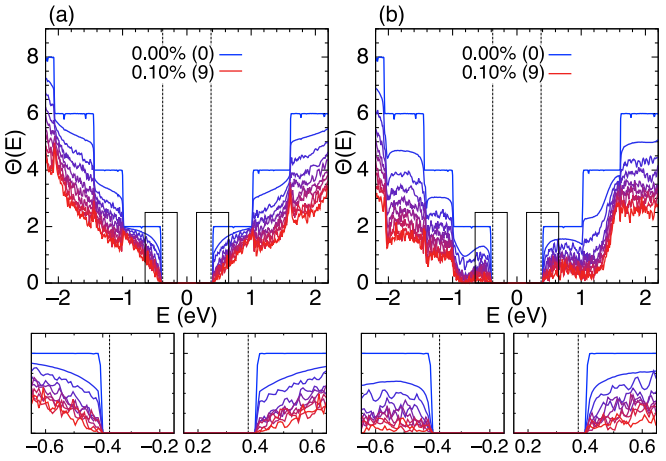

FIG. 3. Transmission function of 100-nm CNTs with (a) vacancies and (b) SW defects. The bottom panels show the transmission of low-energy electrons (closeups of the marked areas). The defect concentration varies from 0.0% (blue) to 0.1% (red) ($N_{\rm def} = 0$ to 9) with the equal interval.

of σ and $\Lambda_{\rm def}$ is proportional to $\sigma^{-\beta}$, we can obtain the fitting equation, $\kappa_{\rm lat}(\sigma) = \kappa_{\rm lat}(0)[1 + \alpha\kappa_{\rm lat}(0)\sigma^{\beta}]^{-1}$ [31], where α and β are fitting parameters. Solid (broken) lines in Fig. 2 show fitting curves for a vacancy (SW defect) with this relationship. In Fig. 2(a), fitting curves for SW defect (broken line) are also shown to compare with data for a vacancy and its inset shows a closeup of the region at high σ.

The introduction of defects significantly decreases $\kappa_{\rm lat}$, particularly at low σ (<0.2 %) for both defects as also shown in previous studies [31,47]; $\kappa_{\rm lat}$ is reduced by half at $\sigma =$ 0.14 %(0.11 %),0.062 %(0.092 %), and 0.060% (0.078%) for 10-, 50-, and 100 - nm CNTs with vacancies (SW defects), respectively. Vacancies decrease $\kappa_{\rm lat}$ of CNTs more effectively than SW defects [29,30] because of the absence of C-C bonds around vacancies, which obviously diminish short-wavelength phonons directly, while their difference is not obvious in short CNTs as shown in Fig. 2(a). Figure 2(a) also shows that, for the SW defect, the dependence of $\kappa_{\rm lat}$ on $L_{\rm def}$, one of the ballistic features of phonon transport [49], remains even at high σ ($\approx$1.0 %) for CNTs with $L_{\rm def} \leqslant$ 100 nm. Sevik *et al.* also show that for longer CNTs (200–600 nm) the length dependence remains to some extent for SW defects of $\sigma = 0.6\,\%$ [47]. On the other hand, the $L_{\rm def}$ dependence of $\kappa_{\rm lat}$ diminishes more rapidly for vacancy: at $\sigma < 0.3\,\%$ for $L_{\rm def} =$ 200−600 nm [47], $\sigma \approx 0.8\,\%$ for $L_{\rm def} =$ 50−100 nm, and $\sigma > 1.0\,\%$ for $L_{\rm def} <$ 50 nm. This result can be understood from the analysis with the atomic Green's function method by Sevik *et al.* [47]. Their analysis shows that phonon MFPs due to vacancy-induced elastic scattering decrease from 100 to 20 nm when σ increases from 0.1% to 1.0% for most phonons (phonons with frequency above 400 cm^{-1}) while MFPs of lower frequency (<200 cm^{-1}) phonons exceed 1 μm even under high σ (≈1.0 %). Therefore, while the $L_{\rm def}$ dependence of $\kappa_{\rm lat}$ diminishes at low σ (≈0.1 %) of vacancies when 100 nm $\leqslant L_{\rm def} \leqslant$ 1 μm, it remains even at high σ (>0.8 %) of vacancies for shorter CNTs ($L_{\rm def} <$ 100 nm) because of the comparable length of MFPs with CNT length. The reason why the ballistic feature is more observable in shorter CNTs (Fig. 2) than in longer CNTs [47] should be the same as the above discussion on vacancy.

IV. ELECTRON TRANSPORT PROPERTIES

A. Transmission function

Since electron contribution to thermoelectric properties is determined by $\Theta(E)$ as shown in Eqs. (2)–(7), the change in $\Theta(E)$ due to defects is discussed here. Figure 3 shows $\Theta(E)$ of 100-nm CNTs for (a) vacancies and (b) SW defects with σ varying from 0.0% (blue line) to 0.1% (red line) with the equal interval of σ (corresponding to $N_{\rm def} =$ 0 to 9). The Fermi level is set to 0 eV. Broken lines indicate the peak chemical potentials, μ giving the maximum P [see Fig. 4(d)], for p- or n-type pristine CNT, defined as $\mu_{p/n,0} = -/+0.38$ eV. $\mu_{p/n,0}$ is located at potential levels slightly higher/lower than the valence/conduction band edge ($E = -/+0.41$ eV) [34]. Closeups on the bottom show $\Theta(E)$ at the marked region around $\mu_{p/n,0}$. While both vacancies and SW defects suppress $\Theta(E)$ significantly, their effects on $\Theta(E)$ are different in some aspects. Vacancies selectively suppress $\Theta(E)$ at band edges, corresponding to the energy levels of Van Hove singularities. This selective suppression of $\Theta(E)$ due to vacancy can be attributed to the generation of quasibound states [25,50], which are generated mostly at energy levels near Van Hove singularities (band edges) and suppress $\Theta(E)$ at the corresponding energy levels. On the other hand, SW defects suppress $\Theta(E)$ in the overall energy range somewhat keeping the original steplike feature. Here, in our additional calculation, we observed that bond distortions without adding any defect decrease $\Theta(E)$ at overall energy levels rather than at specific energy levels. This indicates that the suppression of $\Theta(E)$ in the overall energy range due to SW defects can be described by broad areas of bond distortions as illustrated in Fig. 1. These differences between effects of vacancy and SW defect on $\Theta(E)$ mainly affect the change in S due to defects as shown below.

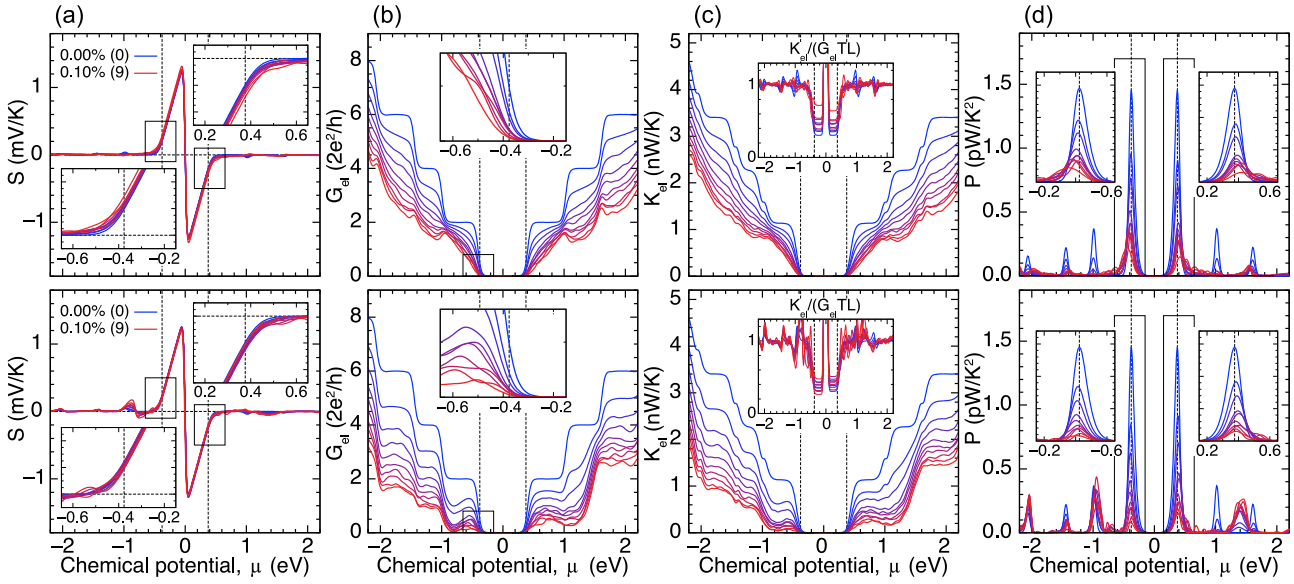

FIG. 4. Thermoelectric properties of 100-nm CNTs with vacancies (top) and SW defect (bottom): (a) Seebeck coefficient, (b) electron conductance, (c) electron thermal conductance, and (d) power factor. Color identification is the same as in Fig. 3. Broken lines denote the peak chemical potentials for P, $\mu_{p/n,\mathrm{opt}} = -/+ 0.38\,\mathrm{eV}$. Insets of (a), (b), and (d) show closeups of the marked region while those of (d) show the Wiedemann-Franz law.

B. Fluctuation of electron contributions to thermoelectric properties

Figure 4 shows different thermoelectric properties, (a) S, (b) G_{el}, (c) K_{el}, and (d) P, of CNTs with vacancies (top) and SW defects (bottom). The range of σ and its color notation are the same as those in Fig. 3. Insets in Figs. 4(a), 4(b), and 4(d) are the closeups around $\mu_{p/n,0}$, denoted by broken lines, while the inset in Fig. 4(c) shows $K_{\mathrm{el}}/(G_{\mathrm{el}}TL)$ with L being the Lorentz number. The introduction of vacancies increases $|S|$ around $\mu_{p/n,0}$ while SW defects do not substantially affect $|S|$ as shown in Fig. 4(a) [this trend can be seen more clearly in Fig. 6(a)]. The trend can be attributed to the aforementioned change in $\Theta(E)$ [34]; while $\partial f/\partial E$, a window function in the denominator of Eq. (5), takes its peak at $E = \mu$, $(\partial f/\partial E)(E-\mu)$, a window function in the numerator of Eq. (5), takes its peak at $E \neq \mu$ ($E = \mu \pm 0.04\,\mathrm{eV}$ for 300 K). In addition, because the former attenuates more rapidly than the latter with increasing $|E-\mu|$, the denominator of Eq. (5) is dominated by $\Theta(E)$ around $E = \mu$ compared with the numerator. Therefore, considering S at $\mu_{p/n,0}$ vacancies, which selectively suppress $\Theta(E)$ near the band edge (near $E = \mu_{p/n,0}$), can mainly reduce the denominator of Eq. (5) and, thus, increase $|S|$. On the other hand, since SW defects decrease $\Theta(E)$ in the overall energy range and decrease both the denominator and the numerator, effects of their changes on S are canceled out and, thus, S does not change substantially. The above discussion allows the further expectation that electron disorders can increase S when the disorders do not cause bond distortion but affect electronic states mainly at the band edge (e.g., adatoms).

While S varies with a relatively complex manner, G_{el} and K_{el} simply follow the change in $\Theta(E)$ as shown in Figs. 4(b) and 4(c); G_{el} and K_{el} decrease with $\Theta(E)$ with increasing σ for both vacancy and SW defect. Compared with the increase in S, the reduction of G_{el} and K_{el} are more significant (also see Fig. 6). This result shows that S is dominated by electronic structures at lead regions, and G_{el} and K_{el} by electron scattering at the defective region. G_{el} and K_{el} near $\mu_{p/n,0}$, the energy range dominating the thermoelectric properties, decrease significantly with increasing σ [inset in Fig. 4(b) for G_{el}]. As for K_{el}, it follows the Wiedemann-Franz law except for around energy levels corresponding to the Van Hove singularities as well as the band gap. The electron contribution to the heat transport, K_{el}, is much less than the lattice contribution, K_{lat}, regardless of σ; for 100-nm CNTs; $K_{\mathrm{el}}(\mu_{p,0})/K_{\mathrm{lat}}$ was 0.09 and 0.01 for $\sigma = 0\,\%$ and 0.1% of the vacancy, respectively.

With increasing defects, P, determined by S and G_{el}, finally reduces significantly as shown in Fig. 4(d) for all cases including the case of vacancy, which enhances $|S|$. This result shows that the enhancement of $|S|$ is overwhelmed by the large reduction of G_{el}, despite P being quadratic to S (linear to G_{el}) (this trend will be discussed again in Fig. 6). Here, one can notice that, with decreasing P, the peak (optimized) chemical potential, $\mu_{p/n,\mathrm{opt}}$, that gives the maximum P for each defective CNT, may shift from $\mu_{p/n,0}$. While it should be appropriate to adopt $\mu_{p/n,0}$ as the representative μ for the pristine CNT, there are two alternatives for defective CNTs: One is to adopt the same $\mu_{p/n,0}$ assuming that μ remains the same in the process of introducing defects, and the other is to take $\mu_{p/n,\mathrm{opt}}$ for each defective CNT reflecting the maximum possible P. Since neither of the representative μ's is universally appropriate and the defects similarly affect p- and n-type CNT properties, in the following, we mainly focus on p-type CNTs and evaluate the properties for both $\mu_{p,0}$ and $\mu_{p,\mathrm{opt}}$ that will be simply denoted by μ_{opt} and μ_0 hereafter.

μ_{opt} indeed changes with increasing σ, particularly for vacancy as shown in Fig. 5(a). For vacancy in a 100-nm

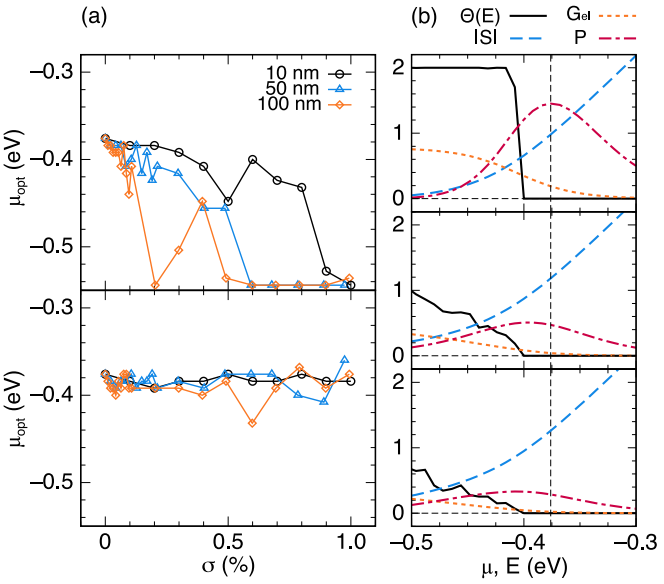

FIG. 5. Peak chemical potential for P shifts with increasing the defect concentration. (a) Fluctuation of the optimized chemical potential for P of p-type CNTs with (top) vacancy and (bottom) SW defect. (b) Change in different electron transport properties for p-type CNTs with vacancies of $\sigma = 0.00, 0.02$, and 0.04% ($N_{\mathrm{def}} = 0, 3$, and 6). The units for $|S|$, G_{el}, P, and $\Theta(E)$ are V/(5000 K), $S/5000$, pW/K^2, and dimensionless, respectively. The competing behavior of G_{el} and S with the introduction of vacancies, the decrease in G_{el}, and increase in S causes the shift of the peak chemical potential for P toward high doping level.

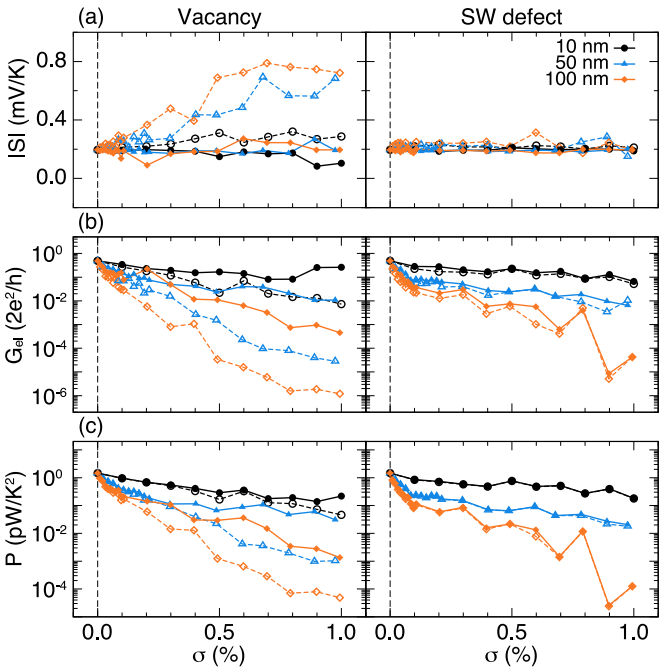

FIG. 6. Thermoelectric properties of CNTs with vacancies (left) and SW defects (right): (a) $|S|$, (b) G_{el}, and (c) P. P and G_{el} are plotted on a logarithmic scale. Solid and broken lines show data at μ_{opt} and μ_0, respectively. Orders of reduction of G_{el} are a dominant factor of the reduction of P due to defects.

CNT, μ_{opt} decreases from $\mu_0(-0.38\,\mathrm{eV})$ and saturates to $\mu = -0.54\,\mathrm{eV}$ at $\sigma \approx 0.5\,\%$. The magnitude of σ at which μ_{opt} saturates increases with increasing L_{def}. This reflects the fact that the same magnitude of σ decreases $\Theta(E)$ more effectively in longer CNTs in the ballistic regime because increasing length for constant σ means larger N_{def}. The change in μ_{opt} can be understood from Fig. 5(b) showing different thermoelectric properties of a 100-nm CNT with $\sigma = 0.00\%, 0.02\,\%$, and 0.04% ($N_{\mathrm{def}} = 0, 3$, and 6). In Fig. 5(b), the units for $|S|$, G_{el}, and P are normalized as V/(5000K), $S/5000$, and pW/K^2, respectively. This figure summarizes the aforementioned trends; with decreasing $\Theta(E)$ due to the introduction of vacancies, S increases (this trend is not clear in this figure because of its slight increase) and G_{el} and P decrease around μ_0. Because of the competing effect of vacancy on S and G_{el} around μ_0, the introduction of vacancies causes the shift of μ_{opt} toward a high-doping level as well as the decrease in the magnitude of G_{el} and P.

The changes in $|S|$, G_{el}, and P with optimizing μ in terms of P are shown in Fig. 6 to clarify impacts of defects on S and G_{el}. Solid and broken lines represent data at μ_{opt} and μ_0, respectively. While $|S|$ increases a few times for vacancy at μ_0 (up to four times for a 100-nm CNT), P decreases with increasing σ (more than four orders of magnitude) because of orders of reduction of G_{el} (up to five orders of magnitude for a 100-nm CNT). While without the optimization of μ the effect of vacancy on thermoelectric properties is larger than that of the SW defect, the μ optimization can recover G_{el} as well as P of CNTs with vacancies up to the same orders or even higher (in the case of a 100-nm CNT) than those of CNTs with a SW defect. Here, it is interesting to note that after the optimization of μ, $|S|$ at μ_{opt} of CNTs with vacancies remains almost constant ($\approx$0.2 mV/K) regardless of σ. In the case of a SW defect (right column of Fig. 6), while the introduction of the defects does not change $|S|$, the significant reduction of G_{el} due to defects (up to five orders of magnitude for a 100-nm CNT) deteriorates P by the same orders as G_{el}. As a result, our findings reveal that the deterioration of P due to the introduction of defects is strongly dominated by the orders of suppression of G_{el} following that of $\Theta(E)$ although $|S|$ increases in the case of vacancy.

C. Figure of merit of individual CNTs

Finally, combining thermal and electron transport properties calculated in the above, we calculated ZT of individual CNTs. Figure 7 shows $Z_{\mathrm{cnt}}T$ of CNTs with (a) vacancies and (b) SW defects of the length of 10 nm (black circle), 50 nm (blue triangle), and 100 nm (orange diamond) at μ_0 (broken line) and μ_{opt} (solid line). Insets show the change in $Z_{\mathrm{cnt}}T$ in the low-σ region with a linear scale. For the pristine CNTs ($\sigma = 0\,\%$), $Z_{\mathrm{cnt}}T$ increases with the CNT length (0.06 for 10 nm, 0.08 for 50 nm, and 0.1 for 100 nm). This is because, for the pristine CNTs, while the electronic transport properties do not depend on the CNT length in the fully ballistic regime, the phonon transport, whose anharmonicity is not negligible even in short CNTs, degrades with increasing the CNT length.

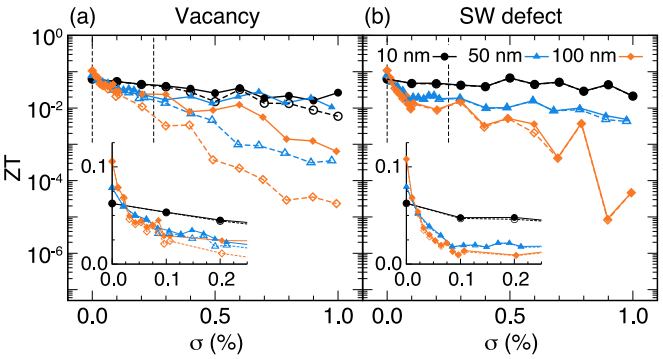

FIG. 7. Figure of merit of CNTs with (a) vacancies and (b) SW defects. Insets show the data at low σ (<0.25%), denoted by broken lines in the main figure, with linear scale. Solid and broken lines show data at μ_{opt} and μ_0, respectively, the same as in Fig. 6.

However, because electronic transport properties, particularly G_{el}, of longer CNTs are fluctuated more sensitively due to defects, $Z_{cnt}T$ of longer CNT reduces more significantly and the length dependence of $Z_{cnt}T$ reverses at $\sigma \approx 0.02\,\%$; i.e., $Z_{cnt}T$ decreases with increasing L_{def} under σ exceeding 0.02%. As a result, while both K_{lat} and P reduce due to defects, the change in $Z_{cnt}T$ due to defects is dominated by electronic properties, particularly G_{el}, which reduces orders of magnitude with increasing σ.

V. THERMOELECTRIC PROPERTIES OF CNT-BASED NETWORKS

Using calculated results in the above, we estimate thermoelectric properties of networks composed of CNTs with vacancies. Firstly, we perform fitting of the electron transmission function and lattice thermal conductivity calculated for single CNTs with empirical functions. For electron transmission function, we adopt a function $\Theta(E,L_{def},\sigma) = \Theta_0(E)/\{1 + L_{def}/L_{mfp}(E,\sigma)\}$ [47], where $\Theta_0(E)$ is the transmission function for the pristine CNT and the energy-dependent elastic mean free path $L_{mfp}(E,\sigma)$ is the fitting parameter. For thermal conductivity, we adopt $\kappa_{lat}(L_{def},\sigma) \propto L_{def}^{t}$, where exponent t is the fitting parameter [51]. Figure 8(a) shows the result

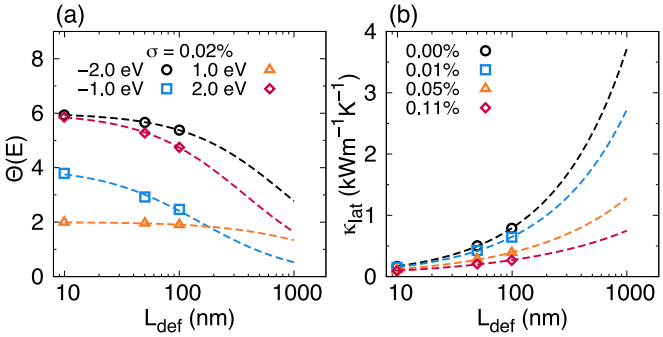

FIG. 8. Fitting results: (a) electron transmission function $\Theta(E,L_{def},\sigma)$ of CNTs with $\sigma = 0.02\,\%$ at different energy levels and (b) thermal conductivity of CNTs with different σ.

of fitting for the electron transmission function of CNTs with $\sigma = 0.02\,\%$ at different energy levels, and Fig. 8(b) shows the result for thermal conductivity with different defect concentrations. The plots show that the fitted functions (dashed lines) reproduce the calculated data (markers). The fitting was performed to allow the possiblity to extrapolate the data as will be discussed later, but otherwise, as the following analysis and dicussion are based on the actually calcaluted data, the fitting merely serves to interplolate the plots.

The thermal conductivity of two- or three-dimensional networks composed of randomly dispersed straight CNTs is calculated as [52,53]

$$\kappa_{net}^{(d)} = \frac{\kappa_{net}^{\infty(d)}}{1 + N_J^{(d)}/(12N_{th})}, \tag{8}$$

where the superscript, (d), denotes the network dimension and $N_{th} = (K_{lat} + K_{el})/K_{cc}$ with K_{cc} being the thermal conductance at intertube junctions. $\kappa_{net}^{\infty(d)}$ and $N_J^{(d)}$ are the thermal conductivity of networks composed of CNTs with infinite thermal conductivity and the mean number of junctions per CNT, respectively. $\kappa_{net}^{\infty(d)}$ can be written as $\kappa_{net}^{\infty(d)} = K_{cc} f^{(d)}(d_{cnt},L_{def},\rho)$ with ρ and $f^{(d)}(d_{cnt},L_{def},\rho)$ being the volume density of CNTs and a function determined by structural factors. $N_J^{(d)}$ is nearly proportional to L_{def} and for two- and three-dimensional networks can be obtained, respectively, as

$$\begin{aligned} N_J^{(2)} &= \frac{2n_s}{\pi}\left(L_{def}^2 + 2\pi d_{cnt}L_{def} + \frac{\pi^2}{2}d_{cnt}^2\right), \\ N_J^{(3)} &= \frac{\pi}{2}n_V d_{cnt}\left({L_{def}}^2 + 4d_{cnt}L_{def} + \frac{8}{3}d_{cnt}^2\right), \end{aligned} \tag{9}$$

where n_S and n_V are the surface and volume number density of CNTs, respectively. Here, we assume $n_S = n_V^{2/3}$ and ρ is fixed at a rather dense value 20% [15], corresponding to 0.35 g/cm^3 for (10, 0) CNTs. We used the same formula and abbreviations (e.g., $N_{el} = G_{el}/G_{cc}$ with G_{cc} being electron conductance at intetutbe junctions) to discuss electrical properties of CNT networks. K_{cc} (=50 pW/K) is calculated with the empirical formula based on NEMD simulations [54] (see Appendix) and experimentally observed G_{cc} (=3.8 μS) with small-diameter SWNTs ($d_{cnt} < 3$ nm) [55] is employed to obtain the electrical conductivity of the networks, $\lambda_{net}^{(d)}$. Because the Seebeck coefficient of CNT networks, S_{net}, is not sensitive to the network condition (e.g., morphology and number of contacts) and is dominated by S of individual CNTs [23], we use S of individual CNTs as S_{net} for simplicity and obtain the figure of merit of networks as $Z_{net}^{(d)}T = S^2\lambda_{net}^{(d)}/\kappa_{net}^{(d)}$. For electron properties (G_{el} and S), values at μ_{opt} are used in this estimation. As for the defect concentration, because the distance between defects ranges from ≈20 nm (for CNTs with relatively high σ [56]) to submicrons (for highly crystalline CNTs fabricated with a CVD method under high-temperature condition [57,58]), we calculate values in the plausible range of σ, in which the effective averaged distance between defects, L_{def}/N_{def}, exceeds ≈10 nm.

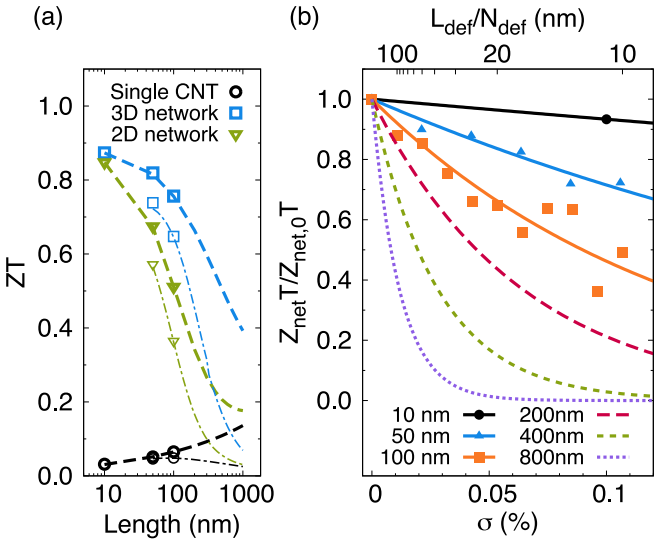

FIG. 9. Figure of merit of CNT-based networks. (a) Figure of merit of individual CNTs (black) and corresponding two- (green) and three- (blue) dimensional CNT networks. Bold and thin lines indicate data for pristine ($\sigma = 0\,\%$) and defective ($\sigma = 0.02\,\%$) CNTs, respectively. (b) Figure of merit of CNT-based three-dimensional networks composed of defective CNTs with different lengths. The data are normalized by values for pristine systems shown in (a).

Using Eqs. (8) and (9) for thermal and electrical conductivity, $Z^{(d)}_{\rm net}T$ can be related to $Z_{\rm cnt}\,T$:

$$Z^{(d)}_{\rm net}T \equiv \alpha^{(d)} Z_{\rm cnt}T, \tag{10}$$

$$\alpha^{(d)} = \frac{N_{\rm th} + N_J^{(d)}/12}{N_{\rm el} + N_J^{(d)}/12}, \tag{11}$$

Equation (11) shows that, when boundaries inhibit thermal transport more effectively than electron transport ($N_{\rm th} > N_{\rm el}$), formation of the network enhances the thermoelectric performance ($Z^{(d)}_{\rm net}T > Z_{\rm cnt}T$); for instance, $N_{\rm th}/N_{\rm el} = 14$ for the 100-nm pristine CNT. In the parameter range of the present calculations, this condition is always satisfied regardless of the CNT length and the introduction of defects. Figure 9(a) shows that formation of the network enhances the figure of merit for both pristine (bold lines) and defective (thin lines) CNTs, where $\sigma = 0\,\%$ and 0.02%, respectively. As for the two-dimensional network, $N_J^{(2)} > N_J^{(3)}$, and thus $Z^{(2)}_{\rm net}T < Z^{(3)}_{\rm net}T$, are satisfied in the realistic range of parameters ($d_{\rm cnt} \leqslant 10\,$nm and $\rho \leqslant 0.35\,{\rm g/cm^3}$), unless the aspect ratio is extremely small ($L_{\rm cnt}/d_{\rm cnt} < 15$).

Figure 9(a) also shows that for a fixed value of σ (=0 % and 0.02 %), $Z^{(d)}_{\rm net}T$ decreases with increasing $L_{\rm def}$ and converges to $Z_{\rm cnt}\,T$. This dependence of $Z^{(d)}_{\rm net}T$ on $L_{\rm def}$ can be observed for the whole range of σ as shown in Fig. 9(b). The general trend can be understood from the fact that, in networks composed of shorter CNTs, phonons and electrons pass through more junctions that enhance the thermoelectric performance. The actual trend can be somewhat more complicated depending on the relative magnitude of each component in Eqs. (10) and (11). However, when electron and thermal transport are ballistic and quasiballistic, respectively, as assumed in this study, $Z^{(d)}_{\rm net}T$ should always increase with shortening CNTs composing the network.

When defects are introduced, $Z^{(d)}_{\rm net}T$ is strongly reduced following the suppression of $Z_{\rm cnt}\,T$ seen in Fig. 7. Note that the introduction of defects leads to competing effects on $\alpha^{(d)}$; decrease in $N_{\rm th/el}$ due to the introduction of defects reduces $\alpha^{(d)}$ while increase in $N_{\rm th}/N_{\rm el}$ due to the stronger reduction of $G_{\rm el}$ compared with $K_{\rm th}$ increases $\alpha^{(d)}$. Consequently, the introduction of defects does not vary $\alpha^{(d)}$ substantially, and thus the extent of the reduction shown in Fig. 9(b) remains similar to that of $Z_{\rm cnt}\,T$. The substantial reduction of $Z^{(d)}_{\rm net}T$ clearly shows the importance of improving the crystallinity of CNTs on CNT-based thermoelectrics. This discussion should be applicable to CNTs even longer than 100 nm, as shown in Fig. 9(b), where the calculated data are extrapolated to a CNT length of 1000 nm, which is about the maximum length that ballistic electron transport persists in pristine systems [40].

These calculations show that the increase in both $L_{\rm def}$ and σ deteriorates the thermoelectric performance because of the decrease in $\alpha^{(d)}$ and $Z_{\rm cnt}\,T$, respectively. Furthermore, the deterioration of the thermoelectric performance of CNT-based networks is more crucial for longer CNTs in (quasi-) ballistic systems. We, thus, obtained important insights for the design of CNT-based thermoelectric devices; improving the crystallinity of CNTs and using shorter CNTs can enhance the thermoelectric performance of CNT-based networks.

VI. CONCLUSIONS

We theoretically investigated effects of defects, vacancies, and SW defects, on the thermoelectric properties of semiconducting CNTs and CNT-based networks. We found that vacancies can increase the Seebeck coefficient of individual CNTs (by up to four times) due to the selective suppression of the transmission function at energy levels corresponding to Van Hove singularities. However, significant suppression of electron conductance regardless of the type of defect (by up to five orders) overwhelms the increase in Seebeck coefficient. As for the comparison of effects of the defects, while the reduction of ZT due to vacancies is larger than that due to SW defects at the fixed chemical potential, since the μ optimization functions more efficiently for vacancy, ZT for vacancy is larger than ZT for SW defect with the μ optimization. Further calculations on effects of defects on thermoelectric performance of CNT-based networks show that the improvement of crystallinity of CNTs and the usage of shorter CNTs can effectively increase the ZT of CNT networks. Our findings show concrete ways to enhance the performance of CNT-based thermoelectric devices.

ACKNOWLEDGMENTS

This study is partially supported by Thermal Management Materials and Technology Research Association (TherMAT) and JSPS KAKENHI Grant No. JP26709009. The numerical calculations in this work were carried out on the facilities of the Supercomputer Center, Institute for Solid State Physics, The University of Tokyo, and the TSUBAME2.5 supercomputer in the Tokyo Institute of Technology.

APPENDIX: THERMAL CONDUCTANCE AT INTERTUBE JUNCTIONS

As derived in Ref. [54], thermal conductance at intertube junctions can be calculated by using the empirical formula

$$K_{cc} = \left(AM_{\text{eff}}^{B} + C\right)N_{\text{eff}}, \tag{A1}$$

where $A = -1.62 \times 10^{-11}\,\text{pW/K}$, $B = 10.86$, and $C = 0.2154\,\text{pW/K}$. N_{eff} and M_{eff} are the total effective number of interatomic intertube interactions and effective interatomic intertube interactions per atom in the contact region, respectively. The contribution from a pair of the ith atom in a tube and the jth atom in another tube is derived by the following Lennard-Jones potential form equation,

$$n(r_{ij}) = \begin{cases} 1, & r_{ij} < r_m \\ 2(r_m/r_{ij})^6 - (r_m/r_{ij})^{12}, & r_m \leqslant r_{ij} \leqslant \mathrm{r_c}, \\ 0, & r_c < r_{ij} \end{cases} \tag{A2}$$

where r_{ij} is the distance between the ith and jth atoms, $r_{\text{m}} = 2^{1/6}\sigma_{\text{int}}$ is the distance corresponding to the minimum of the potential, $\sigma_{\text{int}} = 3.4\,\text{Å}$ is the length parameter of the Lennard-Jones potential, and $r_{\text{c}} = 10\,\text{Å}$ is the cutoff length.

[1] L. D. Hicks, T. C. Harman, X. Sun, and M. S. Dresselhaus, Phys. Rev. B **53**, R10493 (1996).
[2] D. W. Song, W. N. Shen, B. Dunn, C. D. Moore, M. S. Goorsky, T. Radetic, R. Gronsky, and G. Chen, Appl. Phys. Lett. **84**, 1883 (2004).
[3] T. Koga, S. B. Cronin, M. S. Dresselhaus, J. L. Liu, and K. L. Wang, Appl. Phys. Lett. **77**, 1490 (2000).
[4] L. D. Hicks and M. S. Dresselhaus, Phys. Rev. B **47**, 12727 (1993).
[5] L. D. Hicks and M. S. Dresselhaus, Phys. Rev. B **47**, 16631 (1993).
[6] B. Poudel, Q. Hao, Y. Ma, Y. Lan, A. Minnich, B. Yu, X. Yan, D. Wang, A. Muto, D. Vashaee, X. Chen, J. Liu, M. S. Dresselhaus, G. Chen, and Z. Ren, Science **320**, 634 (2008).
[7] M. Sakata, T. Hori, T. Oyake, J. Maire, M. Nomura, and J. Shiomi, Nano Energy **13**, 601 (2015).
[8] A. Miura, S. Zhou, T. Nozaki, and J. Shiomi, ACS Appl. Mater. Interfaces **7**, 13484 (2015).
[9] Y. Nakamura, M. Isogawa, T. Ueda, S. Yamasaka, H. Matsui, J. Kikkawa, S. Ikeuchi, T. Oyake, T. Hori, J. Shiomi, and A. Sakai, Nano Energy **12**, 845 (2015).
[10] A. I. Hochbaum, R. Chen, R. D. Delgado, W. Liang, E. C. Garnett, M. Najarian, A. Majumdar, and P. Yang, Nature **451**, 163 (2008).
[11] M. Kashiwagi, S. Hirata, K. Harada, Y. Zheng, K. Miyazaki, M. Yahiro, and C. Adachi, Appl. Phys. Lett. **98**, 023114 (2011).
[12] T. Hori, G. Chen, and J. Shiomi, Appl. Phys. Lett. **104**, 021915 (2014).
[13] J.-W. Jiang, J.-S. Wang, and B. Li, J. Appl. Phys. **109**, 014326 (2011).
[14] N. T. Hung, A. R. T. Nugraha, E. H. Hasdeo, M. S. Dresselhaus, and R. Saito, Phys. Rev. B **92**, 165426 (2015).
[15] R. S. Prasher, X. J. Hu, Y. Chalopin, N. Mingo, K. Lofgreen, S. Volz, F. Cleri, and P. Keblinski, Phys. Rev. Lett. **102**, 105901 (2009).
[16] K. Esfarjani, M. Zebarjadi, and Y. Kawazoe, Phys. Rev. B **73**, 085406 (2006).
[17] T. Fukumaru, T. Fujigaya, and N. Nakashima, Sci. Rep. **5**, 7951 (2015).
[18] M. Nakano, Y. Nonoguchi, T. Nakashima, and T. Kawai, Jpn. J. Appl. Phys. **54**, 04DN03 (2015).
[19] M. Yang, S. Sasaki, M. Ohnishi, K. Suzuki, and H. Miura, Jpn. J. Appl. Phys. **55**, 04EP05 (2016).
[20] Y. Nakai, K. Honda, K. Yanagi, H. Kataura, T. Kato, T. Yamamoto, and Y. Maniwa, Appl. Phys. Express **7**, 025103 (2014).
[21] M. Ito, N. Okamoto, R. Abe, H. Kojima, R. Matsubara, I. Yamashita, and M. Nakamura, Appl. Phys. Express **7**, 065102 (2014).
[22] H. Kojima, R. Abe, M. Ito, Y. Tomatsu, F. Fujiwara, R. Matsubara, N. Yoshimoto, and M. Nakamura, Appl. Phys. Express **8**, 121301 (2015).
[23] D. Hayashi, T. Ueda, Y. Nakai, H. Kyakuno, Y. Miyata, T. Yamamoto, T. Saito, K. Hata, and Y. Maniwa, Appl. Phys. Express **9**, 025102 (2016).
[24] C. R. Oliver, E. S. Polsen, E. R. Meshot, S. Tawfick, S. J. Park, M. Bedewy, and A. J. Hart, ACS Nano **7**, 3565 (2013).
[25] H. Choi, J. Ihm, S. Louie, and M. Cohen, Phys. Rev. Lett. **84**, 2917 (2000).
[26] T. Ando, J. Phys. Soc. Jpn. **74**, 777 (2005).
[27] H. Matsumura and T. Ando, J. Phys. Soc. Jpn. **70**, 2657 (2001).
[28] A. N. Andriotis, M. Menon, and D. Srivastava, J. Chem. Phys. **117**, 2836 (2002).
[29] T. Yamamoto and K. Watanabe, Phys. Rev. Lett. **96**, 255503 (2006).
[30] J. Che, T. Çagin, and W. A. Goddard III, Nanotechnology **11**, 65 (2000).
[31] N. Kondo, T. Yamamoto, and K. Watanabe, E-J. Surf. Sci. Nanotechnol. **4**, 239 (2006).
[32] M. Ohnishi, K. Suzuki, and H. Miura, AIP Adv. **5**, 047124 (2015).
[33] M. Ohnishi, K. Suzuki, and H. Miura, Nano Res. **9**, 1267 (2016).
[34] Y. Ouyang and J. Guo, Appl. Phys. Lett. **94**, 263107 (2009).
[35] L. Lindsay and D. A. Broido, Phys. Rev. B **81**, 205441 (2010).
[36] S. Plimpton, J. Comput. Phys. **117**, 1 (1995).
[37] R. N. Salaway and L. V. Zhigilei, Int. J. Heat Mass Transfer **70**, 954 (2014).
[38] V. Pereira, A. Castro Neto, and N. Peres, Phys. Rev. B **80**, 045401 (2009).
[39] M. Büttiker, Y. Imry, R. Landauer, and S. Pinhas, Phys. Rev. B **31**, 6207 (1985).
[40] M. Purewal, B. Hong, A. Ravi, B. Chandra, J. Hone, and P. Kim, Phys. Rev. Lett. **98**, 186808 (2007).
[41] J. Shiomi and S. Maruyama, Jpn. J. Appl. Phys. **47**, 2005 (2008).
[42] C. W. Padgett and D. W. Brenner, Nano Lett. **4**, 1051 (2004).
[43] J. Maultzsch, S. Reich, C. Thomsen, H. Requardt, and P. Ordejón, Phys. Rev. Lett. **92**, 075501 (2004).
[44] M. Mohr, J. Maultzsch, E. Dobardžić, S. Reich, I. Milošević, M. Damnjanović, A. Bosak, M. Krisch, and C. Thomsen, Phys. Rev. B **76**, 035439 (2007).
[45] E. Pop, D. Mann, Q. Wang, K. Goodson, and H. Dai, Nano Lett. **6**, 96 (2006).

[46] A. Cao and J. Qu, J. Appl. Phys. **112**, 013503 (2012).
[47] C. Sevik, H. Sevinçli, G. Cuniberti, and T. Çağın, Nano Lett. **11**, 4971 (2011).
[48] X. Li, K. Maute, M. L. Dunn, and R. Yang, Phys. Rev. B **81**, 245318 (2010).
[49] J. Shiomi and S. Maruyama, Phys. Rev. B **73**, 205420 (2006).
[50] M. Brandbyge, J.-L. Mozos, P. Ordejón, J. Taylor, and K. Stokbro, Phys. Rev. B **65**, 165401 (2002).
[51] G. Zhang and B. Li, J. Chem. Phys. **123**, 114714 (2005).
[52] A. N. Volkov and L. V. Zhigilei, Phys. Rev. Lett. **104**, 215902 (2010).
[53] A. N. Volkov and L. V. Zhigilei, Appl. Phys. Lett. **101**, 043113 (2012).
[54] R. N. Salaway and L. V. Zhigilei, Phys. Rev. B **94**, 014308 (2016).
[55] M. S. Fuhrer, J. Nygård, L. Shih, M. Forero, Y.-G. Yoon, M. S. C. Mazzoni, H. J. Choi, J. Ihm, S. G. Louie, A. Zettl, and P. L. McEuen, Science **288**, 494 (2000).
[56] G. D. Saraiva, A. G. S. Filho, G. Braunstein, E. B. Barros, J. M. Filho, E. C. Moreira, S. B. Fagan, D. L. Baptista, Y. A. Kim, H. Muramatsu, M. Endo, and M. S. Dresselhaus, Phys. Rev. B **80**, 155452 (2009).
[57] S. Li, Z. Yu, C. Rutherglen, and P. J. Burke, Nano Lett. **4**, 2003 (2004).
[58] Y. Fan, B. R. Goldsmith, and P. G. Collins, Nat. Mater. **4**, 906 (2005).